metals

MDPI

Article

The Effect of Post-Heat Treatments on Microstructure and Mechanical Properties of a L-PBF CoCrNi–AlTi Medium-Entropy Alloy

Xiaojing Xiong [1,2], Xiaodong Nong [1,*], Libin Yu [1], Xianzhao Meng [1], Chunjia Mo [1], Yunjie Bi [1] and Hui Ding [2,*]

[1] Institute of Advanced Additive Manufacturing, Ji Hua Laboratory, Foshan 528200, China
[2] School of Materials Science and Engineering, Southeast University, Nanjing 211100, China
* Correspondence: nongxd@jihualab.ac.cn (X.N.); hding@whu.edu.cn (H.D.)

Abstract

A CoCrNi-AlTi medium-entropy alloy was fabricated via laser powder bed fusion (L-PBF), and its microstructural evolution and mechanical response during aging at 500–900 °C for 1 h were systematically investigated. The as-built alloy exhibits a hierarchical microstructure consisting of elongated columnar grains and dislocation-rich cellular substructures, which is associated with an excellent strength–ductility combination (YS: 848 MPa, UTS: 1136 MPa, EF: 32.6%). Upon aging, a pronounced precipitation-hardening response is observed, with a peak hardness of 501 ± 7 HV and an ultimate tensile strength of 1429 MPa achieved at 800 °C. TEM and STEM-EDS analyses indicate that Ti preferentially segregates along dislocation networks and grain boundaries at early aging stages, promoting the heterogeneous nucleation of nanoscale Ni–Al–Ti–rich precipitates that effectively impede dislocation motion. At elevated aging temperatures, additional Cr-enriched regions with diffuse compositional partitioning are observed within the FCC matrix, occurring concurrently with the peak mechanical performance. Further aging at 900 °C leads to strength degradation, which is attributed to precipitate coarsening and recovery-induced dislocation annihilation. These results highlight the critical role of L-PBF-induced defect structures in governing precipitation behavior and the resulting strength–ductility trade-off during post-build heat treatment of CoCrNi-AlTi medium-entropy alloys.

Keywords: additive manufacturing; medium-entropy alloy; microstructure evolution; precipitation strengthening

Check for updates

Academic Editors: Paul Wood and Urvashi Fowdar Gunputh

Received: 17 December 2025
Revised: 22 January 2026
Accepted: 27 January 2026
Published: 3 February 2026

Copyright: © 2026 by the authors. Licensee MDPI, Basel, Switzerland. This article is an open access article distributed under the terms and conditions of the Creative Commons Attribution (CC BY) license.

1. Introduction

Medium entropy alloys (MEAs), occupying the compositional space between traditional binary/ternary alloys and high entropy alloys (HEAs), have attracted substantial interest as a new class of structural materials due to their favorable combination of mechanical properties, phase stability, and thermal resistance [1]. Among the various MEA systems, CoCrNi-based alloys have emerged as a particularly promising subclass owing to their exceptional damage tolerance, work-hardening behavior, and cryogenic ductility [2,3]. These properties originate from their stable face-centered cubic (FCC) structure, high stacking fault energy, and propensity for deformation mechanisms such as dislocation slip and nanotwinning [4,5].

Despite these advantages, conventionally processed CoCrNi alloys frequently suffer from relatively low yield strength, which restricts their applicability in structural and

load-bearing components [6,7]. To overcome this limitation, alloying strategies involving minor additions of Al and Ti have been proposed. These elements not only enhance solid-solution hardening but also facilitate the precipitation of ordered intermetallic phases such as NiAl- or NiAlTi-based compounds, which can effectively impede dislocation motion while preserving the FCC matrix [8–10]. Such precipitation-strengthened MEAs provide a potential pathway to achieve a desirable combination of strength and ductility.

In parallel, additive manufacturing (AM)—and particularly laser powder bed fusion (L-PBF)—has opened a new route for tailoring the microstructure and performance of MEAs. The ultrahigh cooling rates during L-PBF (~10^5–10^6 K/s) generate nonequilibrium features such as fine cellular substructures, high dislocation densities, and solute segregation patterns [11,12]. These unique microstructural fingerprints not only contribute to the superior strength in the as-built state but also strongly affect phase transformation pathways during subsequent heat treatments. In particular, solute trapping, defect-assisted diffusion, and heterogeneous nucleation within dislocation tangles or cellular boundaries can fundamentally alter precipitation kinetics compared with conventionally processed alloys [13].

Recent investigations on L-PBF processed CoCrNi alloys with Al and Ti additions have demonstrated that these systems are capable of forming fine, coherent nanoprecipitates within the face-centered cubic matrix, leading to promising combinations of strength and ductility [14–17]. However, a comprehensive understanding of how L-PBF-induced hierarchical microstructures influence precipitation behavior and mechanical responses during post-build thermal exposure remains incomplete. In particular, the roles of solute redistribution, precipitation evolution, and temperature-dependent compositional partitioning in determining the strength–ductility trade-off have not yet been systematically clarified.

The present study investigates a non-equiatomic $(CoCrNi)_{94}Al_3Ti_3$ medium-entropy alloy fabricated via laser powder bed fusion (L-PBF). To stabilize a single-phase FCC matrix while promoting precipitation hardening, the alloy composition was tailored by increasing the Co content and decreasing the Cr content relative to the equiatomic CoCrNi base, together with the addition of 3 at.% Al and Ti to form nanoprecipitates during aging heat treatment. This FCC-dominated matrix was intentionally preserved because it is essential for maintaining high ductility and strain-hardening capability in CoCrNi-based medium-entropy alloys. The microstructural evolution, precipitation behavior, and corresponding mechanical responses were systematically examined through aging between 500 °C and 900 °C. Particular attention was paid to the dual roles of element segregation in governing precipitation pathways and the resulting trade-off between strength and ductility. These findings offer new insights into the microstructure–property relationships of additively manufactured MEAs and provide guidance for optimizing post-processing strategies.

2. Material and Methods

2.1. Materials Production

A $Co_{37}Cr_{27}Ni_{30}Al_3Ti_3$ (at.%) medium-entropy alloy was first synthesized via vacuum induction melting using high-purity elemental feedstocks. The resulting ingot was remelted and subsequently atomized using a vacuum induction gas atomization (VIGA) system (Ji Hua Laboratory, Foshan, China) under high-purity argon protection (O_2 < 150 ppm). Atomization was conducted through a Laval-type 3.8 mm diameter nozzle at a dynamic gas pressure of 4.2 MPa. The solidified powders were sieved to obtain a particle size fraction of 15–53 μm, yielding a median diameter (D_{50}) of approximately 32.5 μm. Morphological characterization (Figure 1b) revealed that the powders possessed high sphericity, smooth surfaces, and a low fraction of satellite particles, indicating excellent flowability

and suitability for L-PBF processing. Cylindrical tensile specimens (Φ7 × 75 mm) and cubic samples (10 × 10 × 10 mm) for microstructural analysis were fabricated using a L-PBF system (EOS M290, EOS GmbH, Krailling, Germany). All builds were conducted under a flowing high-purity argon atmosphere to suppress oxidation during processing. The substrate was a 316L stainless steel plate preheated to 80 °C to reduce thermal gradients and residual stress accumulation. Process parameters were employed as follows: laser power of 200 W, scan speed of 1000 mm/s, hatch spacing of 100 μm, and layer thickness of 40 μm. A stripe scanning strategy was used, and a 67° rotation was applied between successive layers to minimize texture development and anisotropy. L-PBF parameters were selected to ensure stable processing and high-density samples.

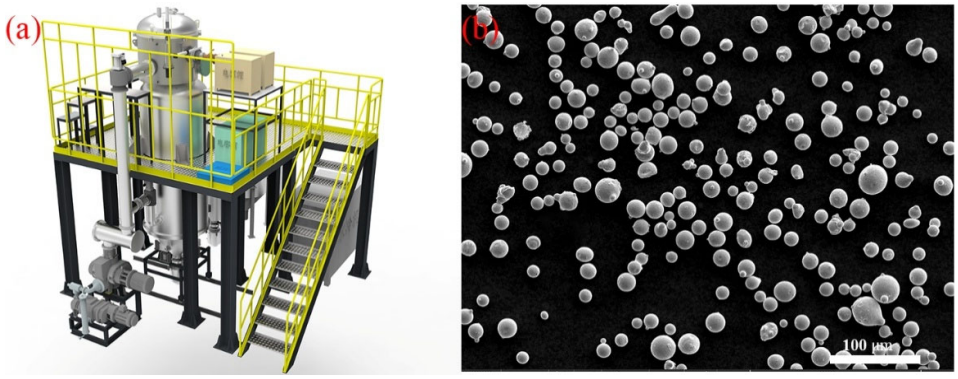


Figure 1. (**a**) Vacuum induction gas atomizer employed for powder fabrication; (**b**) representative SEM micrograph of gas-atomized (CoCrNi)94Al_3Ti_3 powders.

Upon completion of the build, the samples were removed from the substrate using wire electrical discharge machining. To investigate the effects of post-build heat treatment, selected specimens were subjected to thermal exposure at temperatures ranging from 500 °C to 900 °C for 1 h, followed by furnace cooling to room temperature. The heat-treated samples were subsequently used for microstructural characterization and mechanical testing.

2.2. Mechanical Testing

L-PBF fabricated cylindrical samples were precision-machined into dog-bone-shaped tensile specimens with a gauge length of 25 mm and a gauge diameter of 3 mm. Room-temperature uniaxial tensile tests were conducted on an Instron 5982 universal testing machine (Instron, Norwood, MA, USA) at a constant engineering strain rate of 1×10^{-3} s^{-1}. Axial strain was measured using a clip-on Epsilon extensometer with a 25 mm gauge length (Epsilon, Jackson, WY, USA) mounted directly on the gauge section to ensure accurate strain tracking throughout the test.

Vickers microhardness tests were carried out on metallographic cross-sections perpendicular to the build direction (BD) using a QATM QNESS 60A+EVO microhardness tester (QATM GmbH, Bruchsal, Germany) with a load of 500 gf and a dwell time of 10 s. To ensure statistical reliability, ten indentations were performed for each condition and averaged to obtain the reported hardness values.

2.3. Microstructural Characterization

The microstructural evolution was systematically characterized using a combination of electron microscopy techniques. Phase identification and crystallographic analysis were conducted using a field-emission scanning electron microscope (SEM, Thermo Scientific Apreo 2S, Thermo Fisher Scientific, Waltham, MA, USA) equipped with an electron backscatter diffraction (EBSD) detector. Specimens were mechanically ground with SiC

papers (400–2000 grit) and subsequently polished using diamond suspensions, with a final step of 1 μm. Chemical etching was performed in a 5 vol% HNO_3–ethanol solution (Nital) for 10–15 s at room temperature (298 K) to reveal grain boundaries. For EBSD analysis, samples were further electro-polished in a solution of 10 vol% perchloric acid and 90 vol% acetic acid at room temperature under 30 V for ~15 s. EBSD data were processed using the HKL Channel 5 software. The EBSD measurements were conducted with a step size of 0.2 μm, an accelerating voltage of 20 kV, a beam current of 16 nA, and a working distance (WD) of 12 mm.

Nanoscale microstructural features were examined by transmission electron microscopy (TEM) and scanning transmission electron microscopy (STEM) using an FEI Talos F200X (Thermo Fisher Scientific, Hillsboro, OR, USA) operated at 200 kV. Thin foils for TEM analysis were prepared via twin-jet electro-polishing in a solution of 10 vol% perchloric acid and 90 vol% ethanol at ~243 K. The size and distribution of nanoscale precipitates were statistically quantified from at least 30 randomly selected regions using ImageJ software (version 1.53, National Institutes of Health, Bethesda, MD, USA). All TEM and STEM observations were performed on cross-sections perpendicular to the build direction (X–Z plane).

3. Results and Discussion

3.1. Microstructure Analysis

Optical micrographs of the L-PBF CoCrNi-AlTi alloy in the as-built condition are shown in Figure 2. Continuous and well-defined melt pool boundaries are observed in the X–Y (parallel to the substrate, Figure 2a) and X–Z planes (perpendicular to the substrate, Figure 2b), indicating stable and uniform melting–solidification behavior during the L-PBF process. The implementation of a 67° layer-wise rotation scanning strategy gives rise to the characteristic interlaced melt pool morphology. The melt pools exhibit semi-elliptical shapes, with average dimensions of approximately 130 μm in width and 90 μm in depth.

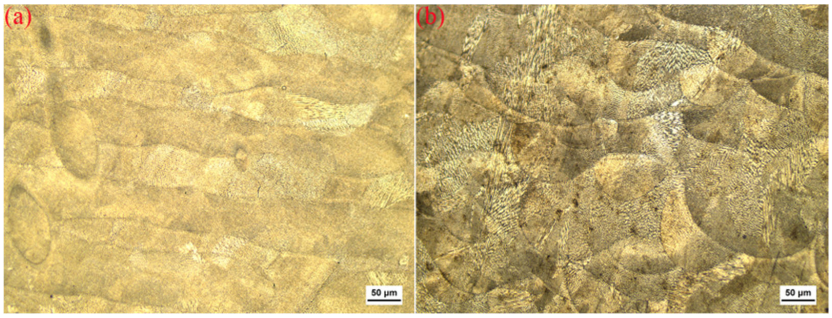


Figure 2. Optical micrographs of the as-built L-PBF CoCrNi-AlTi alloy: (**a**) horizontal and (**b**) transverse cross-section.

EBSD analysis was employed to characterize the grain morphology and local misorientation of the samples (Figure 3). The inverse pole figure (IPF) map of the L-PBF CoCrNi-AlTi alloy in the as-built condition (Figure 3a) reveals elongated grains preferentially aligned along the build direction (BD), which is commonly observed in additively manufactured alloys and is associated with epitaxial grain growth under steep thermal gradients [18,19]. The corresponding kernel average misorientation (KAM) map (Figure 3b) exhibits widespread local misorientations, with an average KAM value of approximately 1.8°, particularly concentrated along sub-grain boundaries. These pronounced local misorientations indicate a high level of lattice distortion and stored defects in the as-built state [20].

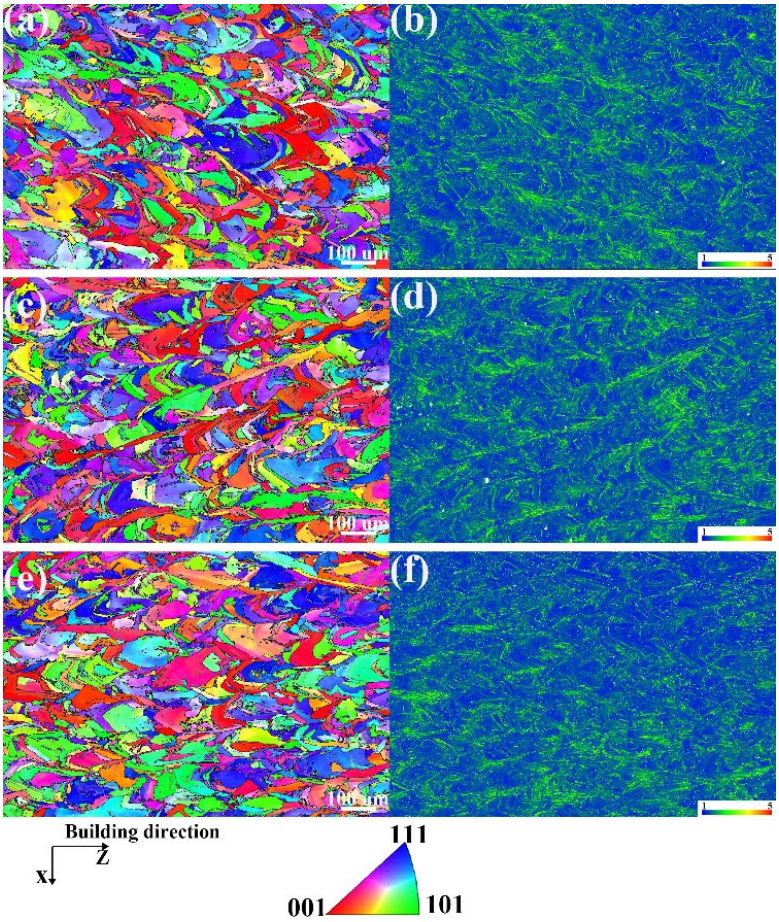


Figure 3. EBSD analysis of the L-PBF CoCrNi-AlTi alloy in the as-built and aged condition: (**a**,**b**) as-built; (**c**,**d**) 500 °C aged; (**e**,**f**) 800 °C aged. Left column: IPF maps along the build direction (BD); right column: KAM maps.

After aging at 500 °C for 1 h, the IPF map (Figure 3c) shows the emergence of locally equiaxed grain regions within the original elongated grain structure. Concurrently, the average KAM value decreases moderately to approximately 1.2°, suggesting a partial relaxation of lattice distortions during thermal exposure. Nevertheless, regions with relatively high local misorientation remain, indicating that a significant fraction of the as-built defect structures is retained after aging at this temperature.

A more pronounced microstructural evolution is observed after aging at 800 °C for 1 h, as shown in Figure 3e. The IPF map reveals a substantial increase in equiaxed grain regions, while the overall columnar grain framework remains discernible at a larger scale. Correspondingly, the average KAM value decreases markedly to approximately 0.8°, reflecting a significant reduction in local misorientation gradients. This microstructural evolution is consistent with thermally activated recovery and the onset of recrystallization under high-temperature exposure [21]. Therefore, the observed decrease in KAM values is interpreted as evidence of defect recovery and local lattice relaxation, rather than unambiguous proof of full recrystallization.

The average grain size was quantified from EBSD maps using the equivalent circular diameter (ECD), where the measured grain area is converted into the diameter of a circle with the same area. The as-built alloy exhibits an average grain size of approximately 20.5 μm. After aging at 500 °C for 1 h, the average grain size slightly decreases to 19.7 μm, while further aging at 800 °C results in a more noticeable reduction to 18.3 μm. This apparent decrease in the EBSD-derived grain size with increasing aging

temperature correlates with the increasing fraction of equiaxed grain regions observed in the EBSD maps, which arises from recovery and partial recrystallization within the original elongated grains. Consequently, the measured grain size evolution reflects EBSD segmentation of newly formed sub-grain regions rather than classical grain refinement or bulk grain growth under the present heat-treatment conditions.

TEM micrographs (Figure 4) provide nanoscale insights into the grain morphology and precipitation behavior of the L-PBF CoCrNi-AlTi alloy after aging. Following aging at 500 °C for 1 h (Figure 4a,b), the microstructure consists of a heterogeneous FCC matrix containing elongated grain regions with lengths of approximately 5–20 μm and widths of 0.3–0.8 μm, together with ultrafine cellular domains ranging from 0.3 to 2 μm. The elongated grains (Figure 4a) exhibit a parallel alignment and are locally decorated by nanoscale particles. Within the cellular regions (Figure 4b), a high density of dislocations is observed, reflecting the non-equilibrium solidification features retained from the L-PBF process. Fine precipitates with an average size of ~40 nm are sporadically distributed within these regions, with a measured number density of approximately 8.9×10^{23} m^{-3}. The limited size and relatively sparse distribution of these particles indicate an early stage of precipitation during aging at 500 °C.

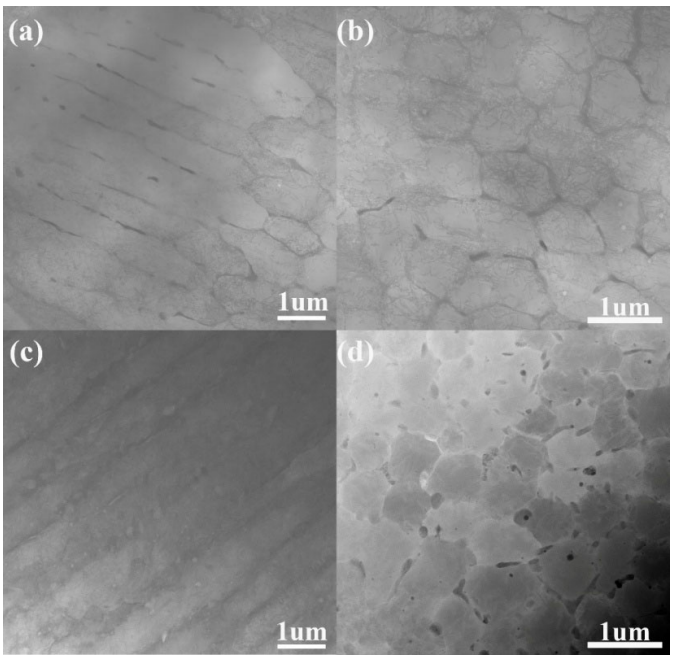


Figure 4. Bright-field TEM images of the L-PBF CoCrNi-AlTi alloy aged for 1 h: (**a**) elongated grain and (**b**) cellular region at 500 °C; (**c**) elongated grain and (**d**) cellular region at 800 °C.

After aging at 800 °C for 1 h, notable changes in precipitation behavior are observed (Figure 4c,d). While the elongated grain framework inherited from L-PBF remains largely preserved in terms of scale and morphology (Figure 4c), the density and size of precipitates increase significantly. Grain boundaries are densely decorated by coarse particles, and intragranular precipitates become more prominent. Meanwhile, the cellular substructure within grains becomes less distinct (Figure 4d), accompanied by a visibly reduced dislocation density.

Quantitative analysis reveals that the average precipitate size increases to approximately 100 nm, while the number density rises to about 2.5×10^{24} m^{-3} after aging at 800 °C. This evolution reflects accelerated precipitation kinetics at elevated temperatures and is consistent with the pronounced hardening response observed at this condition. The concurrent reduction in dislocation density and the presence of closely spaced pre-

cipitates suggest a substantial modification of the deformation substructure during high-temperature aging.

STEM–EDS mapping was employed to examine elemental partitioning and the compositional characteristics of nanoscale features formed during aging. After aging at 500 °C for 1 h, EDS maps acquired from elongated grain regions (Figure 5) reveal an evident enrichment of Ti along grain boundaries, indicating the onset of solute redistribution during thermal exposure.

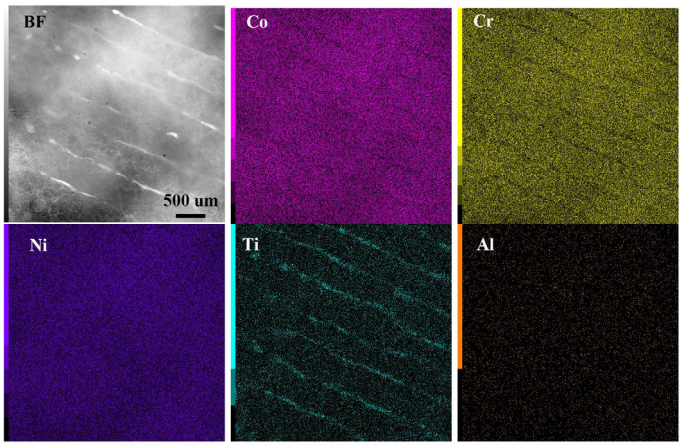


Figure 5. STEM-EDS analysis of the elongated grain region in the L-PBF CoCrNi-AlTi alloy aged at 500 °C for 1 h.

Further analysis of the cellular regions (Figure 6) shows the presence of nanoscale precipitates enriched in Ni, Al, and Ti. These particles are preferentially distributed within regions corresponding to the cellular substructure formed during L-PBF processing, consistent with observations reported for non-equilibrium CoCrNi-AlTi systems [8]. At this aging temperature, the precipitates remain fine and sparsely distributed, suggesting an early stage of precipitation.

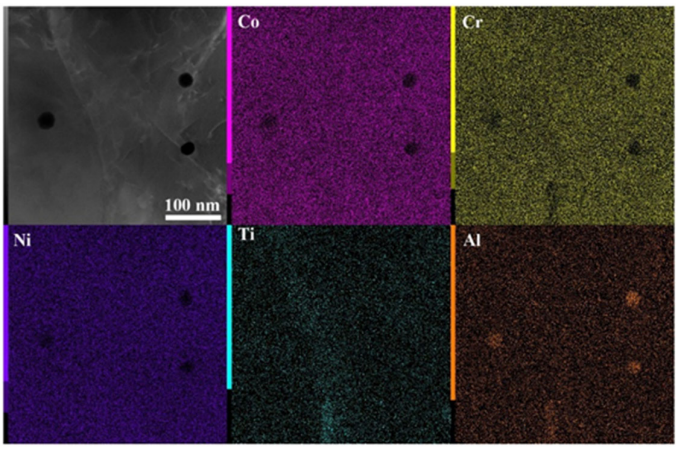


Figure 6. STEM-EDS analysis of the cellular region in the L-PBF CoCrNi-AlTi alloy aged at 500 °C for 1 h.

To further examine the microchemical evolution at elevated aging temperatures, STEM–EDS analysis was conducted on the cellular regions of the L-PBF CoCrNi–AlTi alloy aged at 800 °C for 1 h. As shown in Figure 7, nanoscale precipitates enriched in Ni, Al, and Ti are observed decorating grain boundaries and intragranular regions. Based on their chemical composition and morphology, these particles are identified as Ni–Al–Ti-rich precipitates, consistent with previously reported precipitation behavior in CoCrNi–

AlTi-based systems [22]. In addition to these discrete precipitates, the EDS maps reveal pronounced spatial variations in Cr concentration within the FCC matrix, appearing as broad and diffuse Cr-enriched regions without sharp interfaces. Unlike classical precipitates with well-defined boundaries, these regions exhibit a spatially continuous distribution at the nanoscale. Similar diffuse Cr enrichment has been widely reported in thermally exposed multicomponent FCC alloys [23,24].

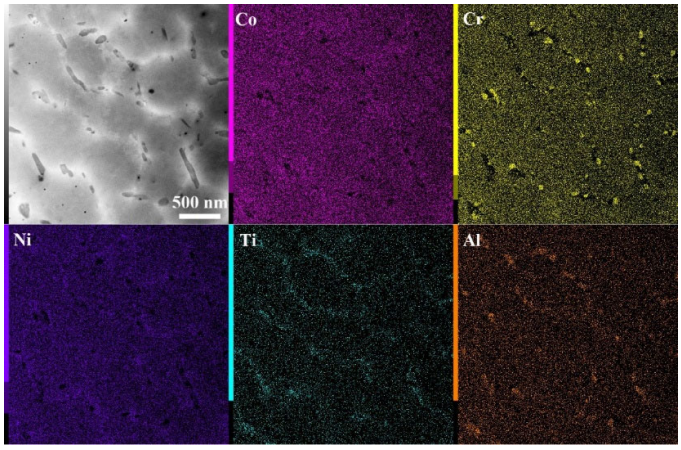


Figure 7. STEM-EDS analysis of the cellular region in the L-PBF CoCrNi-AlTi alloy aged at 800 °C for 1 h.

Further microstructural evolution is observed after aging at 900 °C for 1 h (Figure 8). At this temperature, both the NiTiAl-rich precipitates and the Cr-enriched regions exhibit pronounced coarsening, accompanied by a marked reduction in dislocation density and a degradation in mechanical performance. The simultaneous growth of multiple solute-enriched features reflects the limited thermal stability of the precipitation-hardened microstructure at elevated temperatures, highlighting the trade-off between peak strengthening and high-temperature exposure.

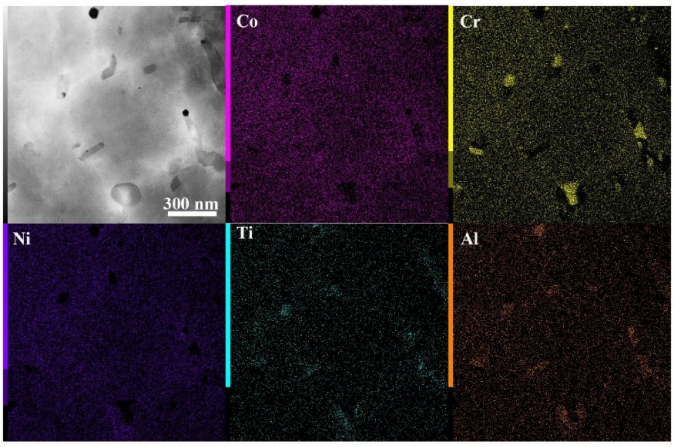


Figure 8. STEM-EDS analysis of the cellular region in the L-PBF CoCrNi-AlTi alloy aged at 900 °C for 1 h.

3.2. Mechanical Properties Evolution During Aging

Figure 9 illustrates the evolution of Vickers microhardness of the L-PBF CoCrNi-AlTi alloy after aging between 500 °C and 900 °C for 1 h. The as-built alloy exhibits the lowest hardness of 339 ± 14 HV, corresponding to a supersaturated FCC solid solution containing a high density of dislocations and fine cellular substructures. Aging at 500 °C results in a

moderate hardness increase to 360 ± 11 HV, which is consistent with the early-stage formation of nanoscale Ti- and Al-containing precipitates along dislocation-rich cellular interiors and grain boundaries, as revealed by TEM (Figure 4) and STEM-EDS (Figure 6). At this stage, precipitation strengthening supplements the dominant solid-solution and dislocation strengthening mechanisms without inducing severe embrittlement. With increasing aging temperature, the hardness increases markedly and reaches a peak value of 501 ± 7 HV at 800 °C. This pronounced hardening response is primarily attributed to the high number density and relatively uniform dispersion of NiTiAl-rich precipitates, which effectively impede dislocation motion [25,26]. In addition, the emergence of continuous Cr-enriched regions within the FCC matrix (Figure 7) introduces additional chemical heterogeneity, further enhancing resistance to dislocation glide. Further aging at 900 °C leads to over-aging, accompanied by a reduction in hardness to 442 ± 9 HV. This softening behavior arises from the coarsening of both NiTiAl-rich precipitates and Cr-enriched regions, together with a substantial decrease in dislocation density (Figure 8), which collectively reduce the effectiveness of precipitation and dislocation strengthening.

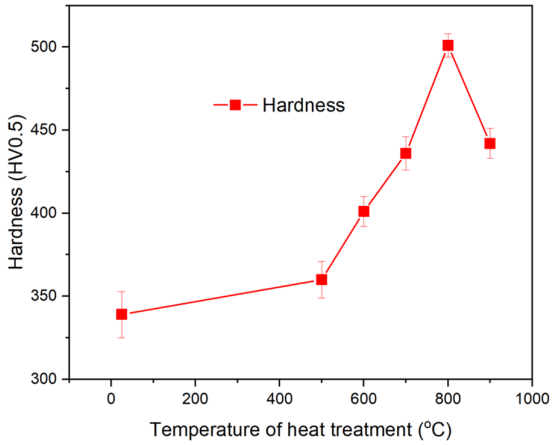


Figure 9. Vickers microhardness of the L-PBF CoCrNi-AlTi alloy after aging at 500–900 °C for 1 h.

Figure 10 presents the engineering stress–strain curves of the L-PBF CoCrNi-AlTi alloy subjected to aging at different temperatures, and the corresponding tensile properties are summarized in Table 1.

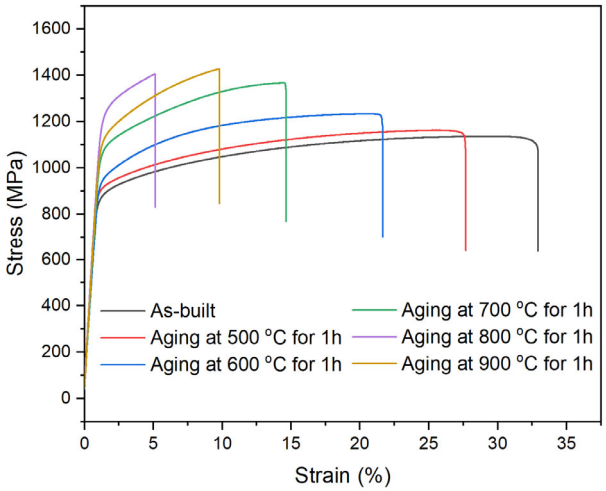


Figure 10. Engineering stress–strain curves of the L-PBF CoCrNi-AlTi alloy after aging at 500–900 °C for 1 h.

Table 1. Tensile properties of the L-PBF CoCrNi-AlTi alloy after aging at 500–900 °C for 1 h, including yield strength (YS), ultimate tensile strength (UTS), and elongation to failure (EF).

Specimens	YS (MPa)	UTS (MPa)	EF (%)
As-built	848	1136	32.6
500 °C 1 h	890	1163	26.5
600 °C 1 h	931	1233	20.28
700 °C 1 h	1054	1367	13.2
800 °C 1 h	1204	1484	6.06
900 °C 1 h	1096	1427	8.34

The as-built alloy demonstrates an excellent strength–ductility balance, with a yield strength (YS) of 848 MPa, an ultimate tensile strength (UTS) of 1136 MPa, and an elongation to failure (EF) of 32.0%. This behavior originates from the hierarchical microstructure formed during L-PBF processing, characterized by dislocation networks embedded within a solute-supersaturated cellular matrix [27]. After aging at 500 °C, both YS and UTS increase slightly to 890 MPa and 1163 MPa, respectively, while EF decreases to 26.5%. The modest strength enhancement reflects the initial precipitation of fine particles within cellular interiors (Figure 4b), which increases resistance to dislocation motion while largely preserving dislocation-mediated plastic deformation [28]. A significant strength enhancement was achieved after aging at 800 °C, with YS and UTS reaching 1094 MPa and 1429 MPa, respectively. However, the ductility dropped drastically to 6.0%. This remarkable increase in yield strength can be quantitatively attributed to precipitation strengthening. For the incoherent or semi-coherent precipitates observed at this stage, the Orowan mechanism is considered dominant. The strengthening contribution ($\Delta\sigma_{\mathrm{Orowan}}$) can be expressed as [29]:

$$\Delta\sigma_{\mathrm{Orowan}} = M\frac{\mathrm{Gb}}{2\pi(1-\nu)\lambda}\ln\left(\frac{r}{b}\right) \quad (1)$$

where M is the Taylor factor (~3.06 for FCC metals), G is the shear modulus, b is the Burgers vector, ν is the Poisson's ratio, $\bar{r}$ is the mean precipitate radius, and λ is the inter-precipitate spacing. Using the measured parameters from TEM analysis ($\bar{r} \approx 50$ nm, $\lambda \approx 100$ nm), the calculated $\Delta\sigma_{\mathrm{Orowan}}$ provides a major contribution to the overall strength increase. The simultaneous drastic loss in ductility is attributed to the limited dislocation storage and plasticity accommodation caused by these densely distributed obstacles.

At 900 °C, a slight decrease in strength (YS: 1096 MPa, UTS: 1427 MPa) and a partial recovery of ductility (EF: 8.3%) were observed. The strength reduction is directly explained by the coarsening of precipitates (Figure 8), which increases the inter-precipitate spacing λ. According to the Orowan equation, an increase in λ leads to a decrease in $\Delta\sigma_{\mathrm{Orowan}}$, diminishing the overall strengthening effect. These changes, combined with recrystallization and dislocation annihilation, which alleviate stress concentration, restore limited plastic deformability while reducing strength. Overall, the mechanical response reflects the competitive interplay between precipitation strengthening, chemical partitioning, and dislocation evolution during thermal aging.

4. Conclusions

This study systematically investigated the microstructural evolution and mechanical behavior of an L-PBF fabricated CoCrNi–AlTi medium-entropy alloy subjected to aging treatments. The main conclusions can be summarized as follows:

1. The as-built alloy exhibits a hierarchical microstructure consisting of columnar grains and dislocation-rich cellular substructures, which provides an excellent strength–ductility balance (YS: 848 MPa, UTS: 1136 MPa, EF: 32.0%) through the

combined effects of solid-solution strengthening, dislocation strengthening, and microstructural heterogeneity.

2. The aging response is strongly influenced by L-PBF-induced defect structures. Dislocation cells and sub-grain boundaries act as preferential sites for heterogeneous nucleation of NiTiAl-rich precipitates, leading to pronounced precipitation strengthening. Peak hardness (501 HV) and ultimate tensile strength (1429 MPa) are achieved after aging at 800 °C, where Orowan bypassing of nanoscale precipitates dominates the strengthening behavior.
3. At elevated aging temperatures (≥800 °C), discrete NiTiAl-rich precipitates coexist with continuous Cr-enriched regions within the FCC matrix, resulting in complex chemical partitioning. Although the underlying phase separation mechanism cannot be conclusively determined based on the present characterization, the coexistence of multiple solute-enriched features plays a critical role in governing the mechanical response.
4. The pronounced strength–ductility trade-off at peak aging conditions arises from the dense distribution of nanoscale precipitates that strongly impede dislocation motion, combined with recovery and partial recrystallization processes that reduce dislocation storage capacity and strain-hardening capability.

The conclusions of this study are based on a fixed aging duration of 1 h and room-temperature mechanical testing. The absence of systematic aging-time-dependent experiments, high-temperature mechanical testing, and diffraction-based phase identification may limit the generality of the proposed strengthening and degradation mechanisms, which will be addressed in future work.

Author Contributions: Conceptualization, X.X. and X.N.; Methodology, X.X. and X.N.; Formal analysis, X.X.; Investigation, L.Y., X.M. and C.M.; Resources, L.Y., X.M. and C.M.; Data curation, X.X.; Writing—original draft, X.X. and X.N.; Writing—review & editing, Y.B. and H.D.; Visualization, X.X.; Supervision, H.D.; Project administration, X.N.; Funding acquisition, X.N. and Y.B. All authors have read and agreed to the published version of the manuscript.

Funding: This study is supported by the National Natural Science Foundation of China (Grant No. 52301148) and Ji Hua Laboratory "Research on aviation-grade high-strength aluminum alloy powder and development of low-cost titanium alloy powder production technology" (Grant No. X200171TM200).

Data Availability Statement: The original contributions presented in this study are included in the article. Further inquiries can be directed to the corresponding authors.

Conflicts of Interest: The authors declare no conflicts of interest.

References

1. Moniri, S.; Yang, Y.; Ding, J.; Yuan, Y.; Zhou, J.; Yang, L.; Zhu, F.; Liao, Y.; Yao, Y.; Hu, L. Three-dimensional atomic structure and local chemical order of medium-and high-entropy nanoalloys. *Nature* **2023**, *624*, 564–569. [CrossRef]
2. He, H.; Wang, Y.; Qi, Y.; Xu, Z.; Li, Y. Review on the preparation methods and strengthening mechanisms of medium-entropy alloys with CoCrNi as the main focus. *J. Mater. Res. Technol.* **2023**, *27*, 6275–6307. [CrossRef]
3. Deng, H.; Wang, M.; Xie, Z.; Zhang, T.; Wang, X.; Fang, Q.; Xiong, Y. Enhancement of strength and ductility in non-equiatomic CoCrNi medium-entropy alloy at room temperature via transformation-induced plasticity. *Mater. Sci. Eng. A* **2021**, *804*, 140516. [CrossRef]
4. Yang, R.; Yang, L.; Wang, T.; Wang, Q. Untra-fine-grained equiatomic CoCrNi medium entropy alloys with high density stacking faults and strengthening mechanisms. *Mater. Sci. Eng. A* **2023**, *870*, 144880. [CrossRef]
5. Xu, D.; Wang, M.; Li, T.; Wei, X.; Lu, Y. A critical review of the mechanical properties of CoCrNi-based medium-entropy alloys. *Microstructures* **2022**, *2*, 2022001. [CrossRef]
6. Liu, J.-P.; Chen, J.-X.; Liu, T.-W.; Li, C.; Chen, Y.; Dai, L.-H. Superior strength-ductility CoCrNi medium-entropy alloy wire. *Scr. Mater.* **2020**, *181*, 19–24. [CrossRef]

7. Ge, J.; Chen, C.; Zhao, R.; Liu, Q.; Long, Y.; Wang, J.; Ren, Z.; Yin, S. Strength-ductility synergy of CoCrNi medium-entropy alloy processed with laser powder bed fusion. *Mater. Des.* **2022**, *219*, 110774. [CrossRef]
8. Li, L.; Song, K.; Gao, Q.; Zhou, C.; Liu, X.; Wang, Y.; Bai, X.; Cao, C. Enhancing strength-ductility synergy of CoCrNi-based medium-entropy alloy through coherent L12 Nanoprecipitates and grain boundary precipitates. *Acta Metall. Sin. (Engl. Lett.)* **2024**, *37*, 78–88. [CrossRef]
9. Cheng, H.; Lu, X.; Zhou, J.; Lu, T.; Sun, B.; Zhang, X.-C.; Tu, S.-T. The influence of L12 ordered precipitates on hydrogen embrittlement behavior in CoCrNi-based medium entropy alloys. *Acta Mater.* **2023**, *260*, 119328. [CrossRef]
10. Yao, N.; Lu, T.; Feng, K.; Sun, B.; Wang, R.-Z.; Wang, J.; Xie, Y.; Zhao, P.; Han, B.; Zhang, X.-C. Ultrastrong and ductile additively manufactured precipitation-hardening medium-entropy alloy at ambient and cryogenic temperatures. *Acta Mater.* **2022**, *236*, 118142. [CrossRef]
11. Zhu, Y.; Zhang, K.; Meng, Z.; Zhang, K.; Hodgson, P.; Birbilis, N.; Weyland, M.; Fraser, H.L.; Lim, S.C.V.; Peng, H. Ultrastrong nanotwinned titanium alloys through additive manufacturing. *Nat. Mater.* **2022**, *21*, 1258–1262. [CrossRef]
12. Gu, D.; Shi, X.; Poprawe, R.; Bourell, D.L.; Setchi, R.; Zhu, J. Material-structure-performance integrated laser-metal additive manufacturing. *Science* **2021**, *372*, eabg1487. [CrossRef]
13. Bi, X.; Li, R.; Yuan, Z.; Cheng, J.; Guan, D.; Zhang, P. Laser-directed energy deposition of a high performance additively manufactured (CoCrNi) 94 (TiAl) 6 medium-entropy alloy with a novel core-shell structured strengthening phase. *Addit. Manuf.* **2024**, *80*, 103971. [CrossRef]
14. Li, Z.; Zhao, P.; Lu, T.; Feng, K.; Tong, Y.; Sun, B.; Yao, N.; Xie, Y.; Han, B.; Zhang, X. Effects of post annealing on the microstructure, precipitation behavior, and mechanical property of a (CoCrNi) 94Al3Ti3 medium-entropy alloy fabricated by laser powder bed fusion. *J. Mater. Sci. Technol.* **2023**, *135*, 142–155. [CrossRef]
15. Wang, J.; Yang, H.; Liu, Z.; Fan, L.; Yan, W.; Qiu, D.; Fu, M. Compositional regulation in additive manufacturing of precipitation-hardening (CoCrNi) 94Ti3Al3 medium-entropy superalloy: Cellular structure stabilization and strength enhancement. *Compos. Part B Eng.* **2024**, *281*, 111570. [CrossRef]
16. Yuan, Z.; Li, R.; Bi, X.; Zhao, S.; Cheng, J. Effects of Ti and Al doping methods on microstructure and properties of laser-directed energy deposited CrCoNi medium-entropy alloys. *Mater. Des.* **2025**, 114416. [CrossRef]
17. Ji, Z.; Qiu, C. Achieving superior high-temperature strength in an additively manufactured high-entropy alloy by controlled heat treatment. *Appl. Mater. Today* **2024**, *40*, 102412. [CrossRef]
18. Liu, Y.; Shi, J. Epitaxial growth and stray grain control toward single-crystal metallic materials by additive manufacturing: A review. *Adv. Eng. Mater.* **2023**, *25*, 2201917. [CrossRef]
19. Li, C.; Jain, M.; Liu, Q.; Cao, Z.; Ferry, M.; Kruzic, J.J.; Gludovatz, B.; Li, X. Multi-scale microstructure manipulation of an additively manufactured CoCrNi medium entropy alloy for superior mechanical properties and tunable mechanical anisotropy. *Addit. Manuf.* **2024**, *84*, 104104.
20. Chandraker, A.; Sharma, K.; Konkati, C.; Barik, S.; Sisodia, S.; Chatterjee, K.; Chauhan, A. Additively manufactured Co–Cr–Ni multi-principal element alloys with excellent strength and ductility at room and cryogenic temperatures. *Virtual Phys. Prototyp.* **2025**, *20*, e2551867. [CrossRef]
21. Yang, L.; Yang, M.; Zhang, Y.; Xie, Q.; Zhang, L.; Chen, Z.; Su, H. Effect of high-temperature heat treatment on mechanical properties and microstructure of CoCrNi medium-entropy alloy formed by laser powder bed fusion. *J. Mater. Res. Technol.* **2025**, *35*, 491–503. [CrossRef]
22. Du, X.; Li, W.; Chang, H.; Yang, T.; Duan, G.; Wu, B.; Huang, J.; Chen, F.; Liu, C.; Chuang, W. Dual heterogeneous structures lead to ultrahigh strength and uniform ductility in a Co-Cr-Ni medium-entropy alloy. *Nat. Commun.* **2020**, *11*, 2390. [CrossRef] [PubMed]
23. Charkhchian, J.; Zarei-Hanzaki, A.; Moshiri, A.; Abedi, H.R.; Schwarz, T.M.; Lawitzki, R.; Schmitz, G.; Chadha, K.; Aranas, C., Jr.; Shen, J. Spinodal decomposition of B2-phase and formation of Cr-rich nano-precipitates in AlCoCrFeNi2. 1 eutectic high-entropy alloy. *Adv. Eng. Mater.* **2023**, *25*, 2300164. [CrossRef]
24. Li, L.; Li, Z.; da Silva, A.K.; Peng, Z.; Zhao, H.; Gault, B.; Raabe, D. Segregation-driven grain boundary spinodal decomposition as a pathway for phase nucleation in a high-entropy alloy. *Acta Mater.* **2019**, *178*, 1–9. [CrossRef]
25. Tang, S.; Chen, G.; Rui, T.; Kou, Z.; Yi, J.; Feng, T.; Zuhailawati, H.; Wilde, G.; Lan, S. Enhancing Strength-Ductility Synergy in Lightweight Complex Concentrated Alloys via Nano-precipitate Tailored Heterostructures. *Acta Mater.* **2025**, 121468. [CrossRef]
26. Fang, J.; Liu, W.; Luan, J.; Jiao, Z. Phase stability and precipitation in L12-strengthened CoCrNi medium-entropy alloys at intermediate temperatures. *J. Phase Equilibria Diffus.* **2021**, *42*, 781–793. [CrossRef]
27. Wang, J.; Zou, J.; Yang, H.; Zhang, L.; Liu, Z.; Dong, X.; Ji, S. Exceptional strength-ductility synergy of additively manufactured CoCrNi medium-entropy alloy achieved by lattice defects in heterogeneous microstructures. *J. Mater. Sci. Technol.* **2022**, *127*, 61–70. [CrossRef]

28. Zhou, H.; Lin, Y.; Chen, F.; Shen, Q. Effect of precipitation behavior on mechanical properties of a Nb-containing CoCrNi-based high-entropy alloy. *Met. Mater. Int.* **2023**, *29*, 674–692. [CrossRef]
29. Gao, X.; Lu, Y.; Zhang, B.; Liang, N.; Wu, G.; Sha, G.; Liu, J.; Zhao, Y. Microstructural origins of high strength and high ductility in an AlCoCrFeNi2. 1 eutectic high-entropy alloy. *Acta Mater.* **2017**, *141*, 59–66. [CrossRef]

Disclaimer/Publisher's Note: The statements, opinions and data contained in all publications are solely those of the individual author(s) and contributor(s) and not of MDPI and/or the editor(s). MDPI and/or the editor(s) disclaim responsibility for any injury to people or property resulting from any ideas, methods, instructions or products referred to in the content.